Using Numerical Dissipation Rate and Viscosity to Assess Turbulence-Related Data Accuracy – Part 1: Experimental Setup

Vojtěch Turek, Zdeněk Jegla*, Miloslav Dohnal, and Marcus Reppich*

DOI: 10.1002/cite.202200044

This is the first part of a two-part paper focusing on the assessment of accuracy of turbulence-related data from computational fluid dynamics (CFD) simulations using effective numerical dissipation rate and effective numerical viscosity. Setup of the CFD cases replicating a swirling pipe flow experiment from literature, for which turbulence-related data measured via laser Doppler anemometry (LDA) had been reported, is presented. The way effective numerical dissipation rate and effective numerical viscosity were obtained for each mesh cell is also discussed. The results of the study are presented in the second part of this series.

Keywords: Computational fluid dynamics, Numerical dissipation, Numerical viscosity, Reynolds stress tensor

Received: April 11, 2022; *revised:* June 22, 2022; *accepted:* August 30, 2022

1 Introduction

Despite the advances in computer hardware and the increasing availability of computational power, direct numerical simulation (DNS) [1] of fluid flow in many cases still is not feasible. Computational fluid dynamics (CFD) models of fluid flow therefore often utilize large eddy simulation (LES) [2] or adaptive methods such as detached eddy simulation (DES) [3] or scale-adaptive simulation (SAS) [4]. Moreover, in engineering, the most common still are (unsteady) Reynolds-averaged Navier-Stokes ((U)RANS) simulations, in which the main source of errors are the utilized turbulence models [5]. This approach is least accurate; however, its popularity stems from it also being least demanding in terms of computational power.

Numerical dissipation in CFD models originates from the discretization of the corresponding partial differential equations and influences the accuracy of the obtained solution data. The errors introduced in this manner into the computation tend to be significant irrespective of the actual order (i.e., formal accuracy) of the utilized numerical methods. The main manifestation of numerical dissipation is numerical viscosity, i.e., artificial change in effective viscosity due to the fact that in each control volume (i.e., cell), the solution is considered to be constant. Another important factor also is how well the cells are "aligned" with the flow [6]. Obviously, estimating the numerical dissipation rate is most important in commercially used URANS simulations which employ low-order methods.

The corresponding research dates back to the early 2000s [7] but recently the topic has gained considerable momentum [8]. The three-dimensional Taylor-Green vortex flow is usually taken as a benchmark (see, e.g., Schranner et al. [9]) because for it there exists the exact analytical solution. Different vortices are sometimes used as well if the necessary data are available [10]. One can also easily find many other studies focusing on numerical dissipation in LES [11] and implicit LES (ILES) [12] models, ILES simulations using adaptive filtering [13], various simplified methods based on DNS [14], or in different numerical solution and velocity interpolation methods [15]. Various studies are, too, available that discuss specific numerical schemes [16] or even the case when completely arbitrary partial differential equations are used [17]. Some of the proposed numerical schemes also provide adaptive numerical dissipation control [18].

Apart from that, one can encounter papers dealing with related topics such as the estimation of round-off errors [19] or the grid-independent solution via Richardson

[1]Dr.-Ing. Vojtěch Turek, [1]Dr.-Ing. Zdeněk Jegla (Zdenek.Jegla@vut.cz), [2]Dipl.-Ing. Miloslav Dohnal, [1,3]Prof. Dr.-Ing. Marcus Reppich (marcus.reppich@hs-augsburg.de)

[1]Brno University of Technology, Faculty of Mechanical Engineering, Institute of Process Engineering, Technická 2, 61669 Brno, Czech Republic.

[2]SVS FEM s.r.o., Trnkova 3104, 62800 Brno, Czech Republic.

[3]Augsburg University of Applied Sciences, Faculty of Mechanical and Process Engineering, An der Hochschule 1, 86161 Augsburg, Germany.

extrapolation [20]. Other studies discuss methods for the evaluation of mesh resolution of LES models [21], explicit filtering in these models when used for grid- and discretization-order-independent prediction of a conserved scalar [22], flow feature aligned mesh generation and adaptation [23], etc. Moreover, the published works are not strictly limited to fluid flow but regularly apply to other fields involving numerical simulations such as linear [24] or nonlinear [25] structural dynamics.

A great disadvantage of many methods for the estimation of numerical dissipation rate is that they require access into the actual CFD solver, which significantly limits their applicability. In contrast, the method proposed by Schranner et al. [9] (see also the follow-up publication [26] providing additional information on the implementation of this method) treats the CFD solver as a black box from which it only takes selected data. The effective numerical dissipation rate is then obtained for each individual cell as the residual of the discretized integral kinetic energy equation. The effective numerical viscosity is computed as well using the same data extracted from the CFD solver.

One of the earlier studies [27] had shown that quantitative knowledge of the numerical dissipation could be employed to better understand results from dissipative CFD codes. The aim of the present paper was to narrow this hypothesis and determine whether the accuracy of solely the turbulence-related solution data could be assessed using effective numerical dissipation rate and effective numerical viscosity. These two metrics were calculated via the procedure described in the abovementioned paper by Schranner et al. [9]. Reference experimental data from laser Doppler anemometry (LDA) measurements of swirling pipe flow were taken from the study by Pashtrapanska et al. [28]. Because the present paper focuses on engineering applications of CFD (e.g., simulations of various process and power industry equipment), adequate SAS and LES models commonly used in such industries were employed. Utilizing the Reynolds stress model (RSM) [29], which would be able to properly handle the turbulence anisotropy often observed in swirling pipe flows, was not considered because of its prohibitively high (in terms of typical engineering CFD simulations) computational demand.

A brief description of the modeled flow system is provided in Sect. 2, while Sect. 3 discusses the meshes utilized in the individual CFD cases as well as the setup of these cases. The quantities that were exported from each CFD case are listed in Sect. 4. The actual solution data are not part of this paper but are presented in the second part of this series [30].

2 Modeled Flow System

The flow system studied by Pashtrapanska et al. [28] comprised a swirl generator and a straight pipe segment with a tripping ring which enhanced turbulence and reduced the development length of the flow (refer to the respective paper for details as well as the description of the LDA measurement procedure). In the present work, five CFD cases corresponding to the mentioned flow system and featuring different quality meshes were evaluated in ANSYS Fluent 2019 R3 [31]. These also included the computation of effective numerical dissipation rate, ε_n, and effective numerical viscosity, ν_n, at the individual cell level using the procedure proposed by Schranner et al. [9].

The flow velocity and Reynolds stress data yielded by the CFD cases were compared to the values reported in [28], and it was investigated whether the relative changes in the discrepancies in these data could be explained by the relative changes in ε_n and ν_n (i.e., the errors introduced by the discretization) when switching from one mesh to another. There were only two notable differences between the evaluated CFD cases and the physical experiment from [28]; namely:

1) Instead of modeling the actual swirl generator together with the pipe segment, the pipe inlet velocity profile providing all three velocity components (axial, radial, and tangential) was directly specified and corresponded to the ratio of the outer circumferential velocity of the swirl generator, $u_{t,wall}$, to the mean flow velocity, u_m, of $N = u_{t,wall}/u_m = 1$ (see [28] for details). Mean turbulent intensity at the pipe inlet (10.48 %) was obtained via a separate CFD simulation of just the swirl generator (see [32] for information on the respective CFD model).
2) The WMLES-based CFD cases (see further) featured a shorter pipe segment – 1 m instead of 5 m – to keep computational times manageable.

To make data comparison possible, interrogation line segments (ILS; see Fig. 1) from $(x_1, y_1, z_{1,L}) = (-D/2, 0, L)$ to $(x2, y2, z_{2,L}) = (D/2, 0, L)$ corresponding to the LDA measurement locations at L/D = 3.0, 10.0, 17.3, 37.3, 44.8, 52.3, 81.7, and 98.4, where L denotes the downstream distance from inlet and D the diameter of the pipe, were added to the CFD models. Interrogation planes (IP; also shown in Fig. 1) were added as well.

3 Mesh Parameters and CFD Setup

Mesh parameters and CFD setup of each case are listed in Tabs. 1 and 2, respectively. The corresponding mesh cross sections are shown in Fig. 2. Because this work focused on engineering applications of CFD where a compromise between data accuracy and computational demand is always sought, k–ω SST SAS (shear stress transport scale-adaptive simulation) [4] and WMLES (wall-modeled large eddy simulation) [33] turbulence models were employed. The former is an advanced scale resolving model with moderate CPU requirements and, according to our experience, is used very often in practice. As for the latter model, it tends to be used in engineering instead of the computationally very intensive LES when greater accuracy than SAS can offer is needed.

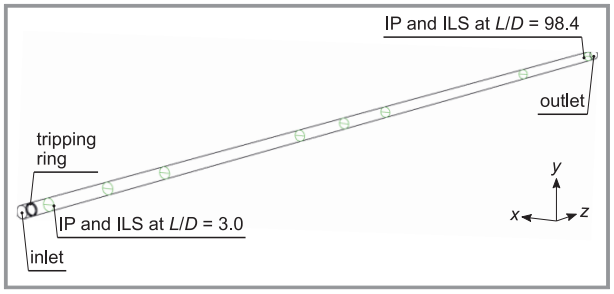

Figure 1. 3D visualization of the investigated flow system; IP and ILS denote interrogation plane and interrogation line segment, respectively. Please note that in the two WMLES-based CFD cases, the computational domains included only the first three interrogation planes and line segments, i.e., only up to L/D = 17.3.

Table 1. Meshes utilized in the individual CFD cases.

Case No.	Cell type	Cell count	Minimum cell orthogonal quality [–]	Maximum cell aspect ratio [–]
1	hexahedral	0.950 million	0.789	3.04
2	hexahedral	1.35 million	0.775	3.20
3	polyhedral	1.94 million	0.241	5.78
4	hexahedral	2.64 million	0.747	3.57
5	hexahedral	20.6 million	0.741	3.93

All model constants have been kept at their default values used by ANSYS Fluent. Repeating here the equations solved by the two utilized models would be of limited benefit and, therefore, the reader is kindly referred to the cited articles [4, 33] or ANSYS Fluent Theory Guide [34] where the equations can easily be found including their derivation and other relevant details.

From Tab. 1 and Fig. 2 it is obvious that no tetrahedral meshes were evaluated. The reason for not considering them was twofold. First, these meshes are more demanding in terms of spatial resolution than hexahedral or polyhedral ones if equivalent accuracy is to be reached. Therefore, in process and power engineering applications of CFD, which often involve simulations of physical phenomena in very large heat exchangers, fired heaters, etc., the general idea is to avoid tetrahedral meshes whenever possible. Second, evaluation of the CFD cases was time-intensive due to the need to collect large amounts of time-dependent data (several weeks to several months of wallclock time per case on a powerful cluster) and, hence, CFD cases not strictly needed to answer the research hypothesis stated in Sect. 1 were not evaluated.

Note that the aim was not to obtain the most accurate solution data possible, but to evaluate the dependence of solu-

Table 2. Main parameters of the evaluated CFD cases.

Parameter	Value (cases 1–3)	Value (cases 4 & 5)
Solver	Pressure-based, transient	Pressure-based, transient
Pressure-velocity coupling	SIMPLEC[a)]	SIMPLEC
Turbulence model	k–ω SST SAS	WMLES[b)]
Gradient	Least squares cell based	Least squares cell based
Spatial discretization	Pressure: 2nd order; momentum: bounded central differencing; turbulent kinetic energy & specific dissipation rate: 2nd order upwind	Pressure: 2nd order; momentum: bounded central differencing
Transient formulation	Bounded 2nd order implicit	Bounded 2nd order implicit
Time step	$2 \cdot 10^{-4}$ s	$5 \cdot 10^{-5}$ s
Scaled residual limits	10^{-3} (all equations)	10^{-3} (all equations)
Walls	No slip, smooth	No slip, smooth
Inlet[c)]	Mass flow inlet	Velocity inlet
Outlet	Pressure outlet	Outflow
Fluid	Diesel oil (physical properties set as per [28])	Diesel oil (physical properties set as per [28])

a) Semi-implicit method for pressure-linked equations (SIMPLE) consistent [35]; b) the WMLES implementation in the utilized version of ANSYS Fluent combines a mixing length model with a modified Smagorinsky model and the wall damping function of Piomelli [34]; c) as mentioned earlier, the axial (streamwise), radial, and tangential components were set via an inlet profile to match the flow field at the outlet from the swirl generator at $N = u_{t,wall}/u_m = 1$, while the mean turbulent intensity was set to 10.48 %.

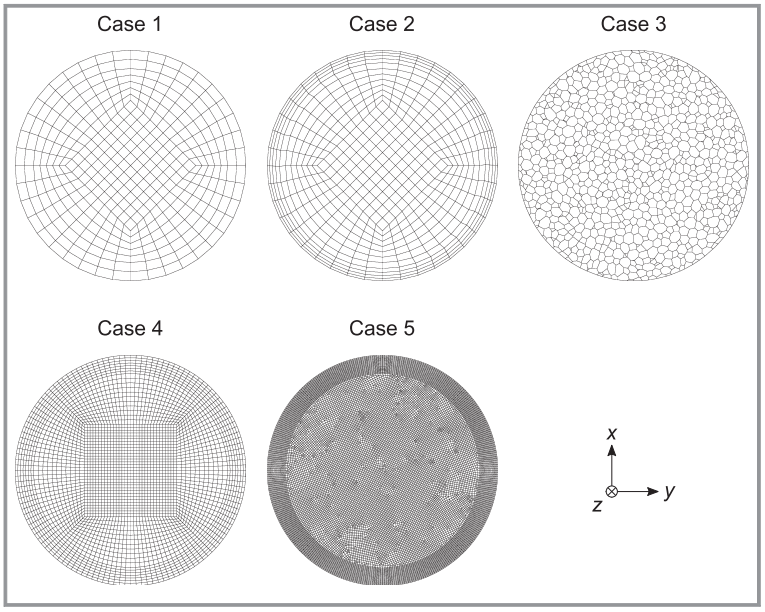

Figure 2. Mesh cross sections in the five evaluated CFD cases. In case 1, the mesh cross section consisted of five structured blocks, while in cases 2 and 4 it consisted of nine structured blocks. Case 3 used unstructured polyhedral mesh with a single block spanning the entire cross section. In the last case (case 5), mesh cross section was composed of four structured blocks in the perimeter and one unstructured (paved hexahedral) block in the core. Only conformal mesh interfaces were used whenever the cross section consisted of more than one block. Please note that the central hexahedral block in case 4 was rotated by 45° compared to cases 1 & 2 to better understand the effect of the core hexahedral cells alignment with the interrogation line segments on the measured quantities.

tion data accuracy on effective numerical dissipation rate and effective numerical viscosity. That is why some of the meshes were intentionally made coarser. For the same reason, no attempt was made to properly resolve the boundary layer in each mesh – especially in case 1 (hexahedral mesh) and case 3 (polyhedral mesh). As for case 3 in particular, it was evaluated primarily to confirm that cell type had significant influence on the values of effective numerical dissipation rate and effective numerical viscosity even if the actual cell count was kept similar.

The effect of the mesh boundary layer itself (i.e., the height of the first cell layer and the corresponding cell growth factor) also was not studied, because it would not help to answer the research hypothesis. Although having well-resolved boundary layers might have led to a slight improvement in data accuracy, it would not significantly change the character of the turbulent flow core. Moreover, according to Menter [36], the k–ω SST SAS model is not sensitive to y^+ while the maximum cell edge length should be at most $0.05D$, where D denotes the characteristic diameter (i.e., the diameter of the pipe). All three meshes used with the respective turbulence model have satisfied this condition. Considering WMLES, ANSYS Fluent Theory Guide states that the required resolution in the wall normal direction is 30–40 cells across half channel height (that is, half the diameter of the pipe). This requirement has been satisfied by both meshes used with WMLES. For the sake of completeness, however, the corresponding condensed y^+ histograms are presented in Fig. 3. Again, note that the meshes intentionally were of lower quality to facilitate data accuracy comparison.

It should also be pointed out that only the flow-related equations were solved, i.e., the continuity and momentum equations plus any other equation required by the utilized turbulence model. Since the influence of viscous dissipation

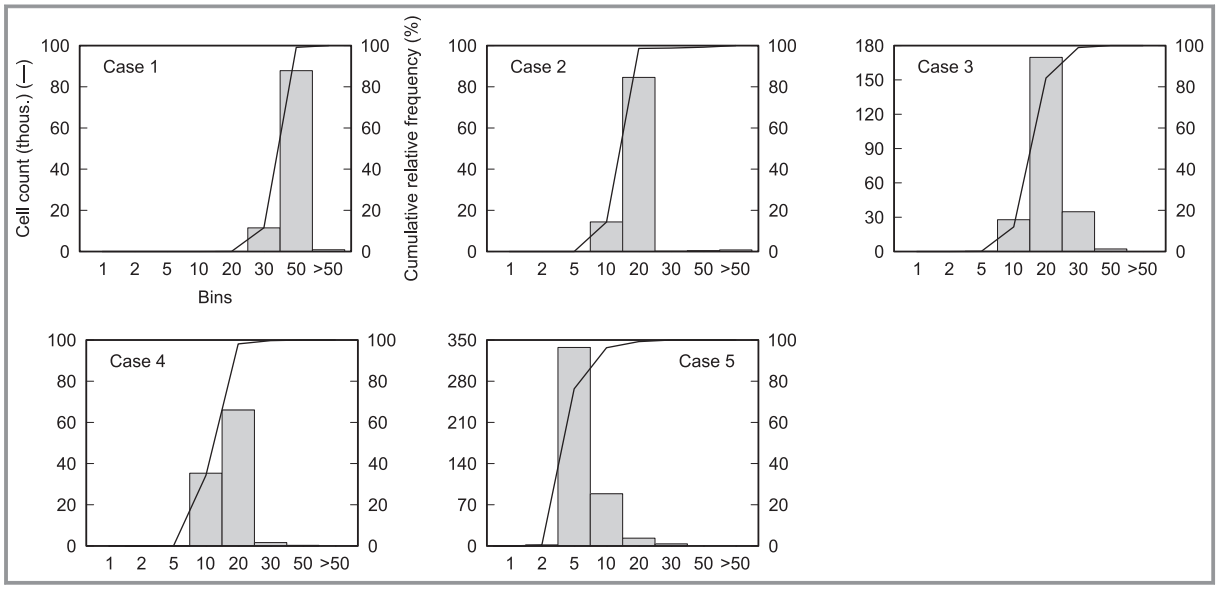

Figure 3. Condensed histograms of y^+ values for wall-adjacent cells in the individual CFD cases.

on flow field was expected to be negligible and the fluid properties were set as constant (i.e., independent of temperature), the energy equation was disabled.

4 Evaluated Quantities

The time-averaged quantities exported from the evaluated CFD cases at each interrogation line segment or interrogation plane corresponded to those available in the paper by Pashtrapanska et al. [28] and were as follows:

- normalized mean velocity profiles (exported at each ILS),
- normalized mean distributions of the diagonal and off-diagonal components of the Reynolds stress tensor (exported at each ILS),
- mean distributions of the effective numerical dissipation rate and effective numerical viscosity (exported at each IP).

Apart from that, also the time-averaged total effective numerical dissipation rates and effective numerical viscosities per the entire computational domains and the corresponding volume-weighted means of time-averaged cell values were considered as potential error level indicators.

In each CFD computation, the initialization period of three residence times (ca. 6.4 s) was followed by a measurement period, during which the averaged quantities were obtained. The length of the measurement period was seven residence times (ca. 15.0 s) in cases 1–4 or three residence times in the last case involving the most detailed mesh. That corresponded to measurement periods consisting of 74 760 time steps or 128 160 time steps, respectively.

Because the density of the fluid was assumed constant, components of the Reynolds stress tensors in the cases involving the k–ω SST SAS turbulence model (1–3) were calculated using

$$\tau_{ij}^{''} = \overline{u_i' u_j'} \tag{1}$$

where i, j denote the axial (streamwise, "a"), radial ("r"), and tangential ("t") components of the velocity vector, $\overline{()}$ time averaging, and $u_i' = u_i - \overline{u_i}$ velocity fluctuations (i.e., the differences between the instantaneous velocities, u_i, and their average values, $\overline{u_i}$). In the cases utilizing the WMLES model (case 4 & 5), the components of the Reynolds stress tensors were obtained as suggested by Bae and Lozano-Durán [37] via

$$\tau_{ij}^{''} = \overline{u_i' u_j'} + \tau_{ij}^{SGS} = \overline{u_i' u_j'} - \nu_t \left(\frac{\partial \tilde{u}_i}{\partial x_j} + \frac{\partial \tilde{u}_j}{\partial x_i} \right) \tag{2}$$

in which τ_{ij}^{SGS} denotes the deviatoric part of the subgrid-scale (SGS) stress tensor approximated using the anisotropic minimum dissipation (AMD) model [38], ν_t the eddy viscosity, $\widetilde{()}$ filtered velocities, and x_i the respective axial (streamwise), radial, and tangential directions. The actual time averaging was carried out internally in ANSYS Fluent through its data sampling capability.

Computation of both the instantaneous and mean effective numerical dissipation rate and effective numerical viscosity for each cell was done via user-defined functions (UDF), which implemented the procedure proposed by Schranner et al. [9]. Please note that neither the source codes of the utilized UDF nor the ANSYS Fluent case and data files are publicly available.

5 Conclusions

In this first part of the two-part series, the studied flow system was presented together with the setup of the respective CFD cases. Reasons were provided regarding the quality of the meshes and the utilized cell types as well as the selection of numerical methods and turbulence models. The way the two considered metrics, effective numerical dissipation rate and effective numerical viscosity, were obtained also was briefly discussed, and references to the papers where the corresponding procedure is described in detail were provided. For the results of this study, the reader is kindly referred to the second paper of the series [30].

Acknowledgment

This research was funded by the Czech Ministry of Education, Youth, and Sports/EU Operational Programme Research, Development and Education, grant No. CZ.02.1.01/0.0/0.0/16_026/0008413 "Strategic partnership for environmental technologies and energy production". Open access funding enabled and organized by Projekt DEAL.

Symbols used

D	[m]	diameter of the pipe
k	[$m^2 s^{-2}$]	turbulence kinetic energy
L	[m]	downstream distance from the swirl generator
N	[–]	ratio of the outer circumferential velocity of the swirl generator to the mean flow velocity
u	[$m\,s^{-1}$]	instantaneous flow velocity
u'	[$m\,s^{-1}$]	flow velocity fluctuation
$\bar{u}$	[$m\,s^{-1}$]	mean flow velocity
$\tilde{u}$	[$m\,s^{-1}$]	filtered velocity
u_m	[$m\,s^{-1}$]	overall mean flow velocity
$u_{t,wall}$	[$m\,s^{-1}$]	outer circumferential velocity of the swirl generator
x, y, z	[–, m]	directions in the coordinate system, spatial coordinates
y^+	[–]	non-dimensional wall distance

Greek letters

ε_n	$[kg\,m^2s^{-3}]$	effective numerical dissipation rate
ν_n	$[m^2s^{-1}]$	effective numerical viscosity
ν_t	$[m^2s^{-1}]$	eddy viscosity
τ''	$[m^2s^{-2}]$	component of the Reynolds stress tensor
τ_{ij}^{SGS}	$[m^2s^{-2}]$	deviatoric part of the subgrid-scale (SGS) stress tensor
ω	$[s^{-1}]$	turbulence eddy frequency

Sub- and Superscripts

a	axial component
i, j	indices of components
L	at the downstream distance L from the swirl generator
r	radial component
t	tangential component

Abbreviations

AMD	Anisotropic Minimum Dissipation model
CFD	Computational Fluid Dynamics
CPU	Central Processing Unit
DES	Detached Eddy Simulation
DNS	Direct Numerical Simulation
(I)LES	(Implicit) Large Eddy Simulation
ILS	interrogation line segment
IP	interrogation plane
LDA	Laser-Doppler Anemometry
RSM	Reynolds Stress Model
SAS	Scale-Adaptive Simulation
SGS	subgrid-scale
SST	Shear Stress Transport
UDF	User-Defined Functions
(U)RANS	(Unsteady) Reynolds-Averaged Navier-Stokes simulation
WMLES	Wall-Modeled Large Eddy Simulation
SIMPLEC	Semi-Implicit Method for Pressure-Linked Equations (SIMPLE) Consistent

References

[1] S. A. Orszag, *J. Fluid Mech.* **1970**, *41 (2)*, 363–386. DOI: https://doi.org/10.1017/S0022112070000642

[2] J. Smagorinsky, *Mon. Weather Rev.* **1963**, *91 (3)*, 99–164. DOI: https://doi.org/10.1175/1520-0493(1963)091<0099:GCEWTP>2.3.CO;2

[3] M. K. Strelets, in *Proc. of the 39th Aerosp. Sci. Meet. Exhib.*, American Institute of Aeronautics and Astronautics (AIAA), Reston, VA, USA **2001**, AIAA 2001-0879.

[4] F. R. Menter, Y. Egorov, *Flow Turbul. Combust.* **2010**, *85 (1)*, 113–138. DOI: https://doi.org/10.1007/s10494-010-9264-5

[5] H. Xiao, J.-L. Wu, J.-X. Wang, R. Sun, C. J. Roy, *J. Comput. Phys.* **2016**, *324*, 115–136. DOI: https://doi.org/10.1016/j.jcp.2016.07.038

[6] R. Holleman, O. Fringer, M. Stacey, *Int. J. Numer. Methods Fluids* **2013**, *72 (11)*, 1117–1145. DOI: https://doi.org/10.1002/fld.3774

[7] C. H. Marchi, A. F. C. da Silva, *Numer. Heat Transf. Part B Fundam.* **2002**, *42 (2)*, 167–188. DOI: https://doi.org/10.1080/10407790190053888

[8] Y. Zhu, X. Hu, *J. Comput. Phys.* **2019**, *399*, 108907. DOI: https://doi.org/10.1016/j.jcp.2019.108907

[9] F. S. Schranner, J. A. Domaradzki, S. Hickel, N. A. Adams, *Comput. Fluids* **2015**, *114*, 84–97. DOI: https://doi.org/10.1016/j.compfluid.2015.02.011

[10] B. R. Williams, *Estimating Grid-Induced Errors in Unsteady CFD Solutions Using a Discrete Error Transport Equation*, Ph.D. Thesis, Iowa State University **2009**.

[11] N. Sharan, G. Matheou, P. E. Dimotakis, *J. Comput. Phys.* **2018**, *369*, 148–172. DOI: https://doi.org/10.1016/j.jcp.2018.05.005

[12] M. El Rafei, L. Könözsy, Z. Rana, *Aerospace* **2017**, *4 (4)*, 59. DOI: https://doi.org/10.3390/aerospace4040059

[13] G. Sun, J. A. Domaradzki, *J. Comput. Phys.* **2018**, *359*, 380–408. DOI: https://doi.org/10.1016/j.jcp.2018.01.009

[14] E. M. J. Komen, L. H. Camilo, A. Shams, B. J. Geurts, B. Koren, *J. Comput. Phys.* **2017**, *345*, 565–595. DOI: https://doi.org/10.1016/j.jcp.2017.05.030

[15] E. M. J. Komen, E. M. A. Frederix, T. H. J. Coppen, V. D'Alessandro, J. G. M. Kuerten, *Comput. Phys. Commun.* **2020**, *253*, 107145. DOI: https://doi.org/10.1016/j.cpc.2020.107145

[16] A. Kurganov, Y. Liu, V. Zeitlin, *ESAIM Math. Model. Numer. Anal.* **2021**, *55 (3)*, 713–734. DOI: https://doi.org/10.1051/m2an/2021009

[17] G. Castiglioni, G. Sun, J. A. Domaradzki, *J. Comput. Phys.* **2019**, *397*, 108843. DOI: https://doi.org/10.1016/j.jcp.2019.07.041

[18] A. Krimi, L. Ramírez, S. Khelladi, F. Navarrina, M. Deligant, X. Nogueira, *Water* **2020**, *12 (10)*, 2858. DOI: https://doi.org/10.3390/w12102858

[19] A. Syrakos, A. Goulas, *Int. J. Numer. Methods Fluids* **2006**, *50 (1)*, 103–130. DOI: https://doi.org/10.1002/fld.1038

[20] B. R. Baliga, I. Y. Lokhmanets, *Int. J. Numer. Methods Heat Fluid Flow* **2016**, *26 (3/4)*, 1121–1144. DOI: https://doi.org/10.1108/HFF-10-2015-0445

[21] L. Davidson, *Quality and Reliability of Large-Eddy Simulations II*, ERCOFTAC Series, Vol. 16, Springer, Dordrecht **2011**.

[22] S. Radhakrishnan, J. Bellan, *Comput. Fluids* **2015**, *111*, 137–149. DOI: https://doi.org/10.1016/j.compfluid.2015.01.003

[23] M. J. Harris, *Flow Feature Aligned Mesh Generation and Adaptation*, Ph.D. Thesis, University of Sheffield **2013**.

[24] Y. Ji, Y. Xing, *Arch. Appl. Mech.* **2021**, *91 (9)*, 3959–3985. DOI: https://doi.org/10.1007/s00419-021-01989-z

[25] W. Wang, Q. Xing, Q. Yang, *Appl. Sci.* **2021**, *11 (4)*, 1932. DOI: https://doi.org/10.3390/app11041932

[26] G. Castiglioni, J. A. Domaradzki, *Comput. Fluids* **2015**, *119*, 37–46. DOI: https://doi.org/10.1016/j.compfluid.2015.07.004

[27] F. Cadieux, G. Sun, J. A. Domaradzki, *Comput. Fluids* **2017**, *154*, 256–272. DOI: https://doi.org/10.1016/j.compfluid.2017.06.009

[28] M. Pashtrapanska, J. Jovanović, H. Lienhart, F. Durst, *Exp. Fluids* **2006**, *41 (5)*, 813–827. DOI: https://doi.org/10.1007/s00348-006-0206-x

[29] B. E. Launder, G. J. Reece, W. Rodi, *J. Fluid Mech.* **1975**, *68 (3)*, 537–566. DOI: https://doi.org/10.1017/S0022112075001814

[30] V. Turek, Z. Jegla, M. Dohnal, M. Reppich, *Chem. Ing. Tech.* **2023**, in press. DOI: https://doi.org/10.1002/cite.202200045

[31] *ANSYS Fluent User's Guide, Version 2019 R3*, ANSYS, Inc., Canonsburgh, PA **2019**.

[32] M. Dohnal, J. Hájek, *Chem. Eng. Trans.* **2016**, *52*, 757–762. DOI: https://doi.org/10.3303/CET1652127
[33] M. L. Shur, P. R. Spalart, M. K. Strelets, A. K. Travin, *Int. J. Heat Fluid Flow* **2008**, *29 (6)*, 1638–1649. DOI: https://doi.org/10.1016/j.ijheatfluidflow.2008.07.001
[34] *ANSYS Fluent Theory Guide, Version 2019 R3*, ANSYS, Inc., Canonsburgh, PA **2019**.
[35] J. P. van Doormaal, G. D. Raithby, *Numer. Heat Transf.* **1984**, *7 (2)*, 147–163. DOI: https://doi.org/10.1080/01495728408961817
[36] F. R. Menter, *Best Practice: Scale-Resolving Simulations in ANSYS CFD, Version 1.0*, ANSYS, Inc., Canonsburgh, PA **2012**.
[37] H. J. Bae, A. Lozano-Durán, *Fluids* **2021**, *6 (3)*, 112. DOI: https://doi.org/10.3390/fluids6030112
[38] W. Rozema, H. J. Bae, P. Moin, R. Verstappen, *Phys. Fluids* **2015**, *27 (8)*, 085107. DOI: https://doi.org/10.1063/1.4928700

